

Received August 29, 2019, accepted September 6, 2019, date of publication September 17, 2019, date of current version October 3, 2019.

Digital Object Identifier 10.1109/ACCESS.2019.2941975

Channel Modeling for Satellite Communication Channels at Q-Band in High Latitude

LU BAI¹, CHENG-XIANG WANG^{2,3,4}, (Fellow, IEEE),
GEORGE GOUSSETIS⁴, (Senior Member, IEEE), SHANGBIN WU⁵,
QIUMING ZHU⁶, (Member, IEEE), WENQI ZHOU⁷, AND
EL-HADI M. AGGOUNE⁸, (Senior Member, IEEE)

¹Shandong Provincial Key Laboratory of Wireless Communication Technologies, School of Information Science and Engineering, Shandong University, Qingdao 266237, China

²National Mobile Communications Research Laboratory, School of Information Science and Engineering, Southeast University, Nanjing 210096, China

³Purple Mountain Laboratories, Nanjing 211111, China

⁴Institute of Sensors, Signals and Systems, School of Engineering and Physical Sciences, Heriot-Watt University, Edinburgh EH14 4AS, U.K.

⁵Samsung R&D Institute U.K., Staines-upon-Thames TW18 4QE, U.K.

⁶College of Electronic and Information Engineering, Nanjing University of Aeronautics and Astronautics, Nanjing 211106, China

⁷Shandong Huahan Electronics Company Ltd., Jinan 250101, China

⁸Sensor Networks and Cellular Systems Research Center, University of Tabuk, Tabuk 47315/4031, Saudi Arabia

Corresponding author: Cheng-Xiang Wang (chxwang@seu.edu.cn)

This work was supported in part by the National Key Research and Development Program of China under Grant 2018YFB1801101, in part by the National Natural Science Foundation of China (NSFC) under Grant 61960206006, in part by the Fundamental Research Funds for the Central Universities under Grant 2242019R30001, in part by the Taishan Scholar Program of Shandong Province, and in part by the EU H2020 RISE TESTBED project under Grant 734325.

ABSTRACT This paper proposes a three-dimensional (3D) channel model for satellite communications at Q-band in a high latitude, including the path loss, shadowing, and small-scale fading. The shadowing effect is modelled by a Markov chain. The three states in the Markov chain are separated by the threshold of the received power level for the link budget and system optimization. The probability density function (PDF) of shadowing amplitude is modelled by a mixture of two Gaussian distributions with parameters obtained by the expectation-maximum (EM) algorithm. The small-scale fading is represented by a 3D geometry-based stochastic model (GBSM) where scatterers are located on the spherical surface of a hemisphere. The movement of the receiver and the Rician factor influenced by environment scattering are considered. Statistical properties including the local temporal autocorrelation function (ACF) and Wigner-Ville spectrum are derived. The satellite communication channel measurement at Q-band is conducted on the campus of Heriot-Watt University (HWU) in Edinburgh, UK. The parameters of our proposed channel model are estimated by the measurement data. Numerical and simulation results demonstrate that our proposed channel model has the ability to reproduce main statistical properties which are also consistent well with the corresponding theoretical and measurement results.

INDEX TERMS Satellite communications, Q-band, Markov chain, GBSM.

I. INTRODUCTION

The fifth generation (5G) wireless communication networks will come to the stage of commercial deployment in 2020. Its system performance, such as data rate, latency, energy efficiency, and cost efficiency, has a great improvement compared to the fourth generation (4G) networks [1]–[4]. However, 5G wireless communication networks are still based on

The associate editor coordinating the review of this manuscript and approving it for publication was Wei Feng.

base stations and cannot achieve the worldwide coverage and overcome the problems of special occasions, e.g., the maritime communication scenario [5], [6] and natural disasters. With the acceleration of beyond 5G (B5G) wireless communication process, satellite communication technologies and unmanned aerial vehicle (UAV) communication technologies have attracted wide attention for their reduced vulnerability of natural disasters and physical attacks [7]–[10]. As a technology that has been proved and deployed for a long time, satellite communications stand out for its capacious service

coverage capabilities. In the past years, satellite communications have been widely used for a variety of applications such as navigation, earth observations, and broadcasting. There are higher requirements for satellite communication systems, such as the higher capacity, improved quality of service (QoS), and ubiquitous connectivity, when there is considerable interest in the application of next generation terrestrial wireless communication systems. For the design and performance evaluation of satellite communication systems, it is necessary to get a general, accurate, and low-complexity model to depict the underlying realistic propagation channel characteristics [11].

Most researchers mainly focus on using different distributions to represent the shadowing and small-scale fading and how the shadowing affects the line-of-sight (LoS) and scattered components. The authors in [12]–[16] used Rayleigh distribution and lognormal distribution to model small-scale fading and shadowing, respectively. In [12] and [13], the authors associated the above two distributions as additive. The envelope of LoS component faded by shadowing and multipath scattered component are assumed independent with each other. The phases are also independent with each other. The major difference between [12] and [13] is that the LoS component in [13] is Doppler shifted, so the model in [13] has a higher degree of freedom. The authors in [14]–[16] took the association of the two distributions as multiplicative. The envelope of multipath scattered component is effected by shadowing and LoS component is ignored in [14]–[16]. The channel models in [17]–[21] used Nakagami-m/Nakagami-q distribution instead of Rayleigh distribution to model small-scale fading because they represent more diverse fading conditions compared to Rayleigh distribution. As Rayleigh distribution is a special case of Nakagami family distributions, the channel models in [17]–[20] are viewed as generalizations of the multiplicative Rayleigh-lognormal models in [14]–[16].

Aforementioned channel models composed of two distributions are oversimplified and not flexible to depict the channel characteristics under kinds of weather conditions and environments separately and clearly. For classifying different channel states and describing the received power level changes over time, the Markov chain process has been widely used to model satellite communication channels, such as [12], [16], [22]–[25]. It defines specified number of states with specified probability depending only on the previous state. The authors in [22] modeled the satellite propagation fading channels by hidden Markov models of 10 states. The number of states was too large to explain the physical mechanism of these states. Meanwhile, the International Telecommunication Union (ITU) recommended it is better to use a three-state model to depict the satellite signal propagation [30]. A dynamic higher order Markov state model for multiple satellite broadcasting systems was proposed in [12]. The hidden Markov models and dynamic higher order Markov state models provide better balance between complexity and accuracy. The channel models in [12], [23]–[25] proposed

Markov-chain-based channel models for satellite systems at L-band, Ku-band, Ku-band, and X-band, respectively. While the traditional satellite communications service at L-band (1-2 GHz), C-band (4-8 GHz), X-band (8-12 GHz), and Ku-band (12-18 GHz), the increasing need for higher bandwidth for reducing costs drives the exploitation of millimeter wave (mmW) bands. Q-band (33-50 GHz) is used for the feeder link of satellite communication systems in order to free lower band spectrum to revenue user links and reduce cost of the terrestrial segment [26]–[28]. Additionally, compared with 5G wireless communications at mmW bands, satellite communications at Q-band have better performance in global seamless coverage and reliability at disaster scenarios. Although none of [12], [22]–[25] has considered the satellite propagation at Q-band in high latitude, variations at frequency band have a major effect on space-to-earth channel. They used conventional distributions in traditional satellite channel models to generate parameters, such as Rice distribution, lognormal distribution, Nakagami-Rice distribution, Loo distribution, and lognormal-Rayleigh distribution. However, none of them focused on the improvement of parameter estimation algorithm. The current small-scale channel models based on Rayleigh or Nakagami family are insufficient to take the propagation mechanism and the correlations among amplitude, angle, and Doppler frequency into account. The ratio of LoS component to non-line-of-sight (NLoS) component was also not considered.

In this paper, we propose a three-dimensional (3D) channel model for satellite communications at Q-band in a high latitude. The main **contributions** of this paper are summarized as follows:

- 1) The mixture of Gaussian (MoG) distribution is firstly used to depict the satellite shadowing channel model. Expectation-maximum (EM) algorithm is used to estimate parameters of probability density functions (PDFs) of amplitude of Markov chain process states.
- 2) The received power level of the channel is modeled via a Markov process.
- 3) 3D geometry-based channel model (GBSM) is firstly used to model satellite small-scale fading. The correlations among channel parameters (distances of multipaths, azimuth angle of arrival (AAoA), elevation angle of arrival (EAoA), azimuth angle of departure (AAoD), elevation angle of departure (EAoD), Doppler frequency, and phase) are considered. The movements of receiver (Rx) and cluster are also taken into account.
- 4) The measurement data of satellite-to-earth propagation channel at Q-band in high latitude has been obtained and analyzed to model.

The rest of the paper is organized as follows. The 3D channel model for satellite communications at Q-band in high latitude is shown in Section II. In Section III, we describe the measurement setup of satellite communications at Q-band. The parameter estimation via measurement data is also given in this section. The statistical properties of the

TABLE 1. Summary of key parameter definitions.

Symbol	Definition
$h(t)$	Channel impulse response for satellite communication at Q-band in high latitude
$h_1(t)$	FSPL
L	Altitude of the satellite
R_E	Radius of the earth
f_c/c	Carrier frequency/ speed of light
$h_2(t)$	Shadowing and modification of path loss for satellite communication
P	Stationary state probability vector (SSPV)
P_t	State transition probability matrix (SPTM)
$\alpha(t)$	Amplitude of $h_2(t)$
$h_3(t)$	Small-scale fading for satellite communication
f_{\max}^{LoS}	Maximum Doppler frequency of the LoS component
f_{\max}^{NLoS}	Maximum Doppler frequency of the non-line of sight (NLoS) component
$h_3^{\text{LoS}}(t)$	LoS path of small-scale fading
$R(t)$	Radius of the hemisphere
K/S	Rician factor and number of rays within one cluster
$f^{\text{LoS}}(t)$	Doppler frequency of LoS path
$\phi^{\text{LoS}}(t)$	Phase of LoS path
$D^{\text{LoS}}(t)$	Vector from Rx to satellite
$\varphi^{\text{LoS}}(t)$	AAoA of LoS path
$\theta^{\text{LoS}}(t)$	E AoA of LoS path
$h_3^{\text{NLoS}}(t)$	NLoS path of small-scale fading
$f^{\text{NLoS}}(t)$	Doppler frequency of NLoS path
$\phi_s^{\text{NLoS}}(t)$	Phase of NLoS path via the s -th ray
$D_s^{\text{R}}(t)$	Vector from cluster to Rx via the s -th ray
$\varphi_s^{\text{R}}(t)$	AAoA of NLoS path from cluster to Rx via the s -th ray
$\theta_s^{\text{R}}(t)$	E AoA of NLoS path from cluster to Rx via the s -th ray
$D_s^{\text{T}}(t)$	Vector from satellite to cluster via the s -th ray
$\varphi_s^{\text{T}}(t)$	AAoD of NLoS path from satellite to cluster via the s -th ray
$\theta_s^{\text{T}}(t)$	E AoD of NLoS path from satellite to cluster via the s -th ray
v_c	Velocity vector of cluster
φ_c^v	AAoD of movement of cluster
θ_c^v	E AoD of movement of cluster
v	Velocity vector of Rx
φ^v	AAoD of movement of Rx
θ^v	E AoD of movement of Rx

proposed reference model are derived in Section IV. Section V presents the corresponding simulation model. Simulation results and analysis are also given in Section V. At last, conclusions are drawn in Section VI.

II. 3D SATELLITE CHANNEL MODEL

The proposed 3D channel model for satellite communications at Q-band in high latitude can be decomposed into three parts, and can be presented as

$$h(t) = h_1(t) \times h_2(t) \times h_3(t) \quad (1)$$

where $h_1(t)$ and $h_2(t)$ denote the free space path loss (FSPL), and the shadow fading, respectively, $h_2(t)$ is a Markov chain process based on measurement will be explained in Section III, $h_3(t)$ denotes the small-scale fading, which is caused by scattering multipaths and the movement of Rx. The definitions of key parameters for the proposed 3D theoretical satellite channel model are given in Table 1.

A. FSPL

FSPL is mainly determined by the distance and frequency. It predicts how the area mean varies with the distance between the satellite and Rx [31]. FSPL can be expressed as

$$h_1(t) = \sqrt{10^{-\frac{4\pi f_c \|D^{\text{LoS}}(t)\|}{10c}}} \quad (2)$$

where f_c is carrier frequency, c is speed of light, the initial distance D^{LoS} between the satellite and Rx can be calculated by

$$D^{\text{LoS}}(t) = \|D^{\text{LoS}}\| \begin{bmatrix} \cos\varphi^{\text{LoS}}(t) \cos\theta^{\text{LoS}}(t) \\ \sin\varphi^{\text{LoS}}(t) \cos\theta^{\text{LoS}}(t) \\ \sin\theta^{\text{LoS}}(t) \end{bmatrix} \quad (3)$$

with

$$\|D^{\text{LoS}}\| = \sqrt{(R_E^2 \sin^2 \theta^{\text{LoS}} + L^2 + 2LR_E) - R_E \sin \theta^{\text{LoS}}} \quad (4)$$

where $\|D^{\text{LoS}}\|$ is the initial distance between satellite and Rx [29], R_E is the radius of the earth (in the range

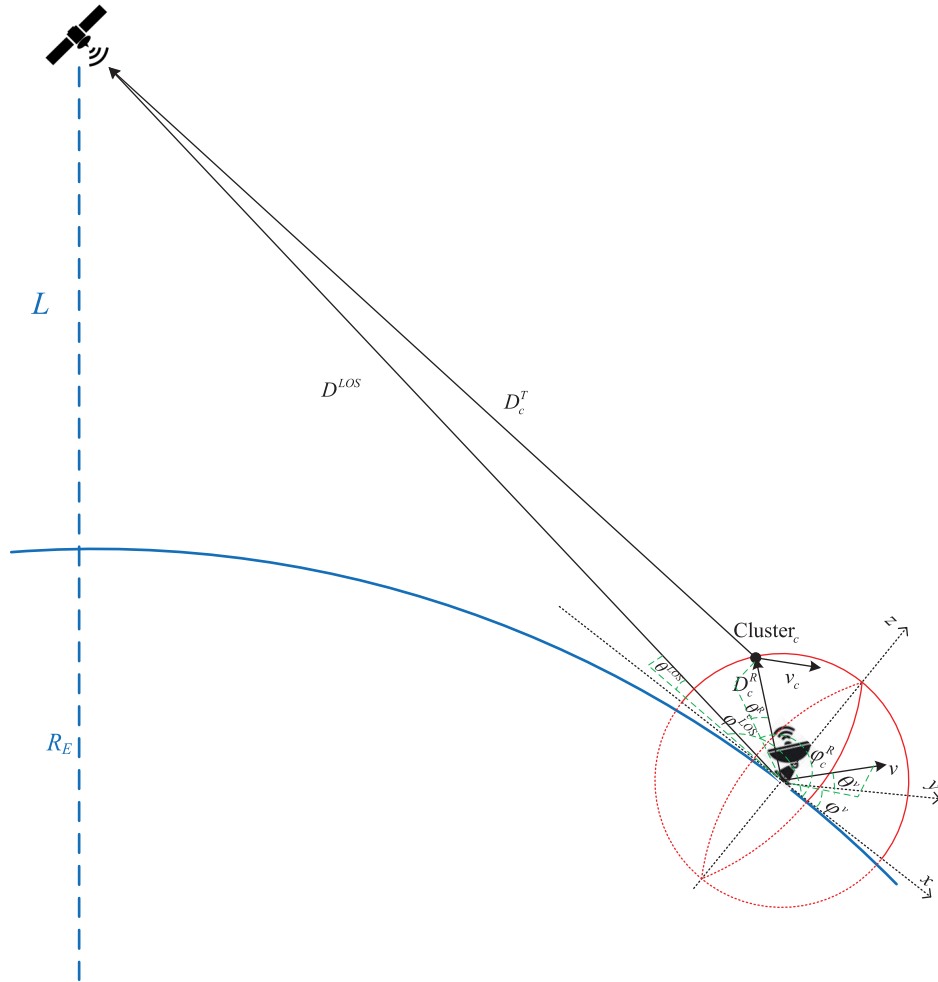


FIGURE 1. The 3D channel model for satellite communication channel at Q-band.

of 6378.1–6356.8 km, depending on the latitude), L and θ^{LoS} respectively present the altitude of the satellite and elevation angle as shown in Fig. 1.

B. SHADOW FADING

The long-term variations of the amplitudes are modeled as a chain of distinct states using a first order Markov-chain process. The differentiated received signal amplitude level is related to the underlying signal propagation condition, which is represented as a state of the Markov model. The bad state corresponds to the situation that the received signal cannot be detected because of the link budget. The moderate state occurs in bad weather conditions, and corresponds to the deep fading which can be detected by the satellite communication receiver system. The good state corresponds to a small signal lever oscillation with low scattering contributions.

The first order Markov model can be represented by a stationary state probability vector (SSPV) which contains the limited probabilities of three states and a state transition probability matrix (SPTM) which contains all transition probabilities between any two of three states. The SSPV is

presented as

$$P = [P_G, P_M, P_B]^T \tag{5}$$

$$P_i = \lim_{N \rightarrow \infty} \frac{N_i}{N}, \quad i \in G, M, B \tag{6}$$

where P_G , P_M , and P_B denote the limited probabilities of good state, moderate state, and bad state, respectively, $[\cdot]^T$ denotes the transpose operator, N_i is the number of the i -th state and N is the total number of three states.

The transitions between any two states are based on SPTM. The state transition diagram of the Markov chain is shown in Fig. 2. The SPTM is presented as

$$P_t = \begin{bmatrix} P_{GG} & P_{GM} & P_{GB} \\ P_{MG} & P_{MM} & P_{MB} \\ P_{BG} & P_{BM} & P_{BB} \end{bmatrix} \tag{7}$$

$$P_{ij} = \lim_{N \rightarrow \infty} \frac{N_{ij}}{N_i}, \quad i \in G, M, B, j \in G, M, B \tag{8}$$

where P_{ij} denotes the transition probability from the i -th state to the j -th state, N_{ij} is the number of the transition from the i -th state to the j -th state.

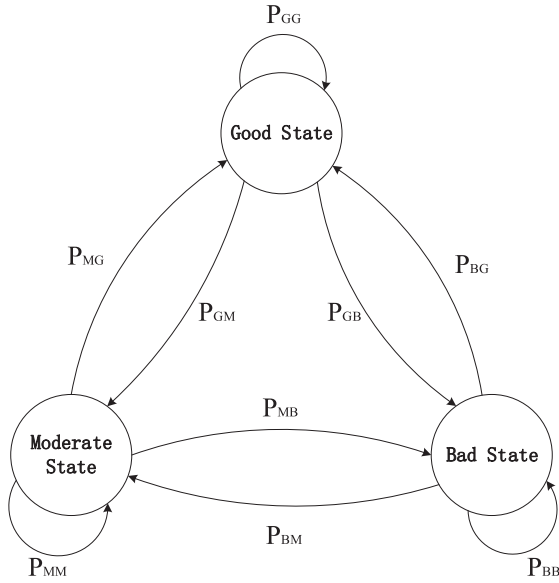


FIGURE 2. The state transition diagram of the Markov chain.

In the measurement data, the number of states is sufficiently large but finite. Therefore,

$$P_i = \frac{N_i}{N}, \quad i \in G, M, B \quad (9)$$

$$P_{ij} = \frac{N_{ij}}{N_i}, \quad i \in G, M, B, j \in G, M, B. \quad (10)$$

C. SMALL-SCALE FADING

In the theoretical small-scale model shown in Fig.1, the Rx is located at the origin point of the 3D reference coordinate system. The cluster is located at the spherical surface of the hemisphere whose center is also located at the original point of the 3D reference coordinate system. The vector of movement of the cluster and Rx, is defined as v_c and v . The maximum Doppler frequency and carrier wavelength are denoted as f_{\max} and λ . Also, let S denotes the total number of rays within a cluster, which obeys a Poisson distribution in the millimeter wave frequency band [32]. The channel impulse response of small-scale fading can be presented as

$$h_3(t) = h_3^{\text{LoS}}(t) + h_3^{\text{NLoS}}(t) \quad (11)$$

$$= \underbrace{\sqrt{\frac{K}{K+1}} e^{j(2\pi \int_0^t f^{\text{LoS}}(\tau) d\tau + \phi^{\text{LoS}}(t))}}_{\text{LoS}} + \underbrace{\sqrt{\frac{1}{K+1}} \lim_{S \rightarrow \infty} \left(\frac{1}{\sqrt{S}} \sum_{s=1}^S e^{j(\int_0^t f_s^{\text{NLoS}}(\tau) d\tau + \phi_s^{\text{NLoS}}(t))} \right)}_{\text{NLoS}}. \quad (12)$$

The Doppler frequency of LoS path is expressed as

$$f^{\text{LoS}}(t) = f_{\max}^{\text{LoS}} \frac{\langle D^{\text{LoS}}(t), v \rangle}{\|D^{\text{LoS}}(t)\| \|v\|} \quad (13)$$

$$= \frac{v}{\lambda} \begin{bmatrix} \cos\varphi^{\text{LoS}}(t) \cos\theta^{\text{LoS}}(t) \\ \sin\varphi^{\text{LoS}}(t) \cos\theta^{\text{LoS}}(t) \\ \sin\theta^{\text{LoS}}(t) \end{bmatrix}^T \begin{bmatrix} \cos\varphi^v \cos\theta^v \\ \sin\varphi^v \cos\theta^v \\ \sin\theta^v \end{bmatrix}. \quad (14)$$

The received phase of LoS path can be expressed as

$$\phi^{\text{LoS}}(t) = \phi_0 + \frac{2\pi}{\lambda} \|D^{\text{LoS}}(t)\|. \quad (15)$$

The Doppler frequency of NLoS path can be calculated as

$$f_s^{\text{NLoS}}(t) = f_{\max}^{\text{NLoS}} \frac{\langle D_s^{\text{R}}(t), (v - v_c) \rangle}{\|D_s^{\text{R}}(t)\| \|(v - v_c)\|} = \frac{\|(v - v_c)\| \langle D_s^{\text{R}}(t), (v - v_c) \rangle}{\lambda \|D_s^{\text{R}}(t)\| \|(v - v_c)\|} \quad (16)$$

where

$$\|D_s^{\text{R}}(t)\| = R(t) \quad (17)$$

$$D_s^{\text{R}}(t) = \|D_s^{\text{R}}(t)\| \begin{bmatrix} \cos\varphi_s^{\text{R}}(t) \cos\theta_s^{\text{R}}(t) \\ \sin\varphi_s^{\text{R}}(t) \cos\theta_s^{\text{R}}(t) \\ \sin\theta_s^{\text{R}}(t) \end{bmatrix} \quad (18)$$

$$v = \|v\| \begin{bmatrix} \cos\varphi^v \cos\theta^v \\ \sin\varphi^v \cos\theta^v \\ \sin\theta^v \end{bmatrix} \quad (19)$$

$$v_c = \|v_c\| \begin{bmatrix} \cos\varphi_c^v \cos\theta_c^v \\ \sin\varphi_c^v \cos\theta_c^v \\ \sin\theta_c^v \end{bmatrix}. \quad (20)$$

The phase of received NLoS path via the s -th ray can be expressed as

$$\phi_s^{\text{NLoS}}(t) = \phi_0 + \frac{2\pi}{\lambda} (\|D_s^{\text{T}}(t)\| + \|D_s^{\text{R}}(t)\|) \quad (21)$$

where

$$D_s^{\text{T}}(t) = D^{\text{LoS}}(t) + D_s^{\text{R}}(t) \quad (22)$$

$$D_s^{\text{T}}(t) = \|D_s^{\text{T}}(t)\| \begin{bmatrix} \cos\varphi_s^{\text{T}}(t) \cos\theta_s^{\text{T}}(t) \\ \sin\varphi_s^{\text{T}}(t) \cos\theta_s^{\text{T}}(t) \\ \sin\theta_s^{\text{T}}(t) \end{bmatrix} \quad (23)$$

$$D^{\text{LoS}}(t) = \|D^{\text{LoS}}(t)\| \begin{bmatrix} \cos\varphi^{\text{LoS}}(t) \cos\theta^{\text{LoS}}(t) \\ \sin\varphi^{\text{LoS}}(t) \cos\theta^{\text{LoS}}(t) \\ \sin\theta^{\text{LoS}}(t) \end{bmatrix}. \quad (24)$$

III. MEASUREMENT SETUP AND PARAMETER ESTIMATION

A. MEASUREMENT SETUP

Alphasat (also referred to as Inmarsat-4A F4) is a geostationary orbit satellite which is located at 25.0°E. Since May 1st, 2016, the Alphasat beacon Rx at Q-band (39.402 GHz) shown in Fig. 3-(a), has been installed at the roof of the Earl Mountbatten Building on the campus of Heriot-Watt University (HWU) in Edinburgh, UK. The azimuth angle and elevation angle of observation is



(a) The Alphasat beacon Rx on the top of a building at HWU.



(b) The relative location of the receiver.

FIGURE 3. The photographs of measurement campaign.

TABLE 2. Satellite location and specifications.

Location Parameters	Specification
Latitude/ Longitude	55.91°N/ 3.32°W
Altitude	130 m
Elevation Angle	21.3° (nom.) +/- 1.2° (track)
Azimuth Angle	147.2° (nom.) +/- 0.5° (track)

approximately 147.2° and 21.3°, respectively. The measurement campaign is a joint effort between HWU and National Aeronautics and Space Administration (NASA) Glenn Research Center (GRC) to characterize the satellite channel attenuation at the Q-band. The location of the Alphasat beacon terminal is shown in Fig. 3-(b). The location information and specifications for the installation site are summarized in Table 2.

The basis design of the AlphaSat beacon receiver at Q-band is similar to the one installed and in operation since April 2014 at the Politecnico di Milano (POLIMI) described in [33]. It is a 0.6 m Q-band Cassegrain reflector with equivalent antenna beamwidths of 0.9°. The independent open-loop tracking systems is used for the antenna to track the inclined orbit of the Alphasat. The first downconversion to a conventional intermediate frequency (IF) of 70 MHz happens within the temperature controlled the radio frequency (RF) installed directly behind the antenna. Independent temperature controls of the low noise amplifier (LNA) is used to maintain a temperature stability of +/- 0.01°C. The LNA has

a noise figure of 2.7 dB, which results in a reduced dynamic range of 35 dB. From the RF box which is installed behind the antenna, the signal is routed to a secondary temperature controlled IF box where the final downconversion stages take place to the 5 MHz IF. The temperature stability of the IF box is maintained to within +/- 0.25°C. The estimated system temperature of the AlphaSat beacon receiver based on the measured component performance is calculated as 908 K. A common ultra-stable 10 MHz reference oscillator drives all local oscillators utilized in the three-stage downconversion process. The system parameters of the AlphaSat beacon receiver system are shown in Table 3.

The 5 MHz IF of the receiver requires modifications in order to maintain similar performance from the frequency estimation routine employed in all NASA GRC-based beacon receivers [34], [35]. The 5 MHz IF signal is sampled by a 12-bit National Instruments 5124 data acquisition (DAQ) card at a sampling frequency of 11.111 MHz. For the 10 Hz data measurement rate, 220 samples are collected for a final fs/N resolution of 10.6 Hz. In order to perform the frequency estimation routine and record the signal power every 0.1 s, it was required to digitally filter and decimate the sampled data by a factor of 32 to reduce processing time. A 50 kHz 10-th order Type 2 Chebyshev digital bandpass filter is employed prior to decimation. The frequency track of the signal is maintained to center the Chebyshev filter at the current tracked frequency. This also allows for tracking of deep fades by reducing the tracking bandwidth window around the nominal beacon IF frequency when the signal strength is reduced to within 10 dB of the noise floor level.

B. MEASUREMENT DATA

We take the measurement data from June 2016 to May 2017. After deleting the invalid data, the time series of received signal power is shown in Fig. 4. The blue line shows the received signal in 1Hz sample rate. For decreasing the complexity of data pre-processing, we get the received signal in 1/60Hz sample rate marked by red dash line. To a certain degree, the fluctuation of the red dash line can show that of the blue line. The dark line and green dash line show the signal mean power and the signal power after FSPL and losses of the Alphasat beacon terminal system, respectively. The light blue dash line is the minimum detection of signal power. The PDF of the received signal power is shown in Fig. 5.

C. STATE DURATION AND THRESHOLD

According to the performance of satellite system and link budget [36], we set the threshold to distinguish the good state and the moderate state (TGM) by 3 dB, 4 dB and 5 dB lower than signal maximum (-61.844 dB) and the threshold between moderate state and bad state (TMB) as 10 dB lower than TGM. For the resolution and accuracy, we set up the state duration (SD) as 10 min, 15 min, 20 min, 25 min, and 30 min. The PDFs of signal amplitudes of good state, moderate state and bad state with different SDs and TMBs are shown as follows.

TABLE 3. The parameters of AlphaSat beacon receiver.

Receiver Parameters	Performance Specification
Antenna Gain	45.6 dBi
EIRP ($P_{tx}+G_{tx}$ -Losses)	59.5 dBm
L_{fr} (Rx antenna feed losses)	0.2 dB
L_r (Rx antenna depointing losses)	1 dB
IF Amplifier Gain	20 dB (29 dB meas.)
Low-Noise Amplifier Gain	35 dB (38 dB meas.)
Rx C/N (dB,Carrier to Noise ratio)	45.76 dB
Detection Threshold (The minimum C/No for signal detection)	10 dB
Dynamic Range (Demonstrated)	35.76 dB
Q-band Mixer Loss	9 dB
1st Stage Bandpass Filter (20.2 GHz) Loss	1 dB
IF Bandpass Filter (70 MHz) Loss	2.7dB (1.5dB meas.)
IF Lowpass Filter Loss	1.8dB (1.0dB meas.)
Measurement Sampling Rate	1Hz

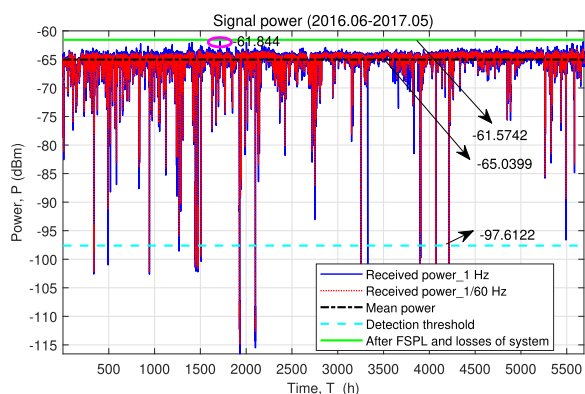


FIGURE 4. The time series of the received signal power.

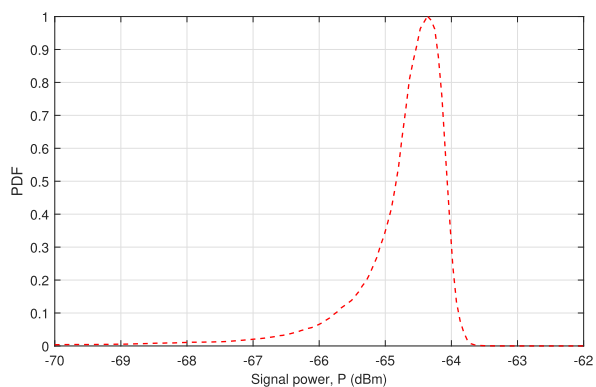
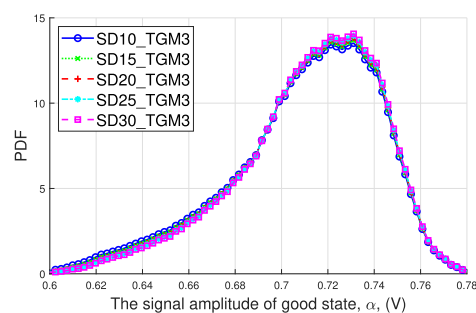


FIGURE 5. The PDF of the received signal power.

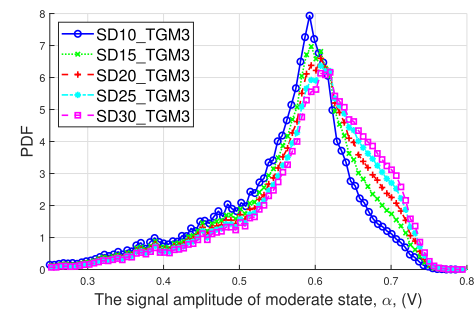
The comparison among Fig. 6, Fig. 7, and Fig. 8 indicates the PDF of signal amplitudes for moderate state is smoother and more stable when the TGM is set up as 3 dB and the SD is set up as 10 min or 15 min. The SSPVs and SPTMs with different TGM and SD which are shown in Table 4.

D. PARAMETER ESTIMATION

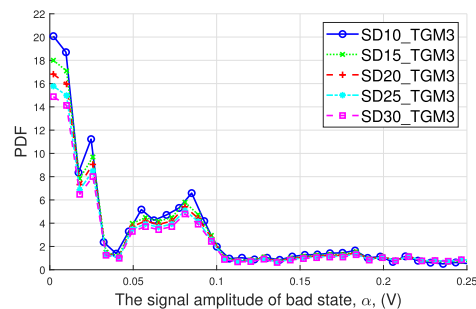
By analyzing the measurement data, we model the PDF of good state as an mixture of two Gaussian distribution, which



(a) Good state.



(b) Moderate state.



(c) Bad state.

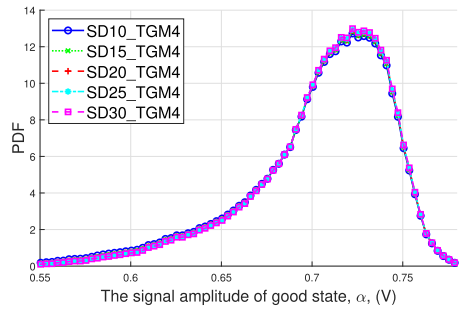
FIGURE 6. The PDFs of signal amplitudes of good state, moderate state and bad state (SD=10, 15, 20, 25, 30 min; TGM=3 dB).

is presented as

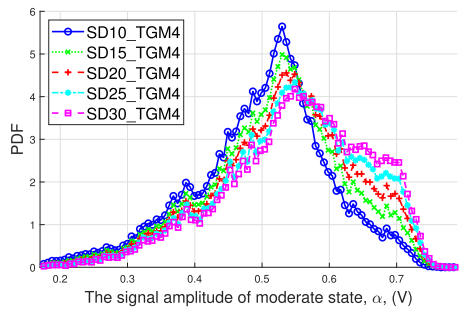
$$p(\alpha) = \sum_{k=1}^2 \omega_k \mathfrak{N}(\alpha; \mu_k, \delta_k^2) \tag{25}$$

TABLE 4. The SSPVs and SPTMs.

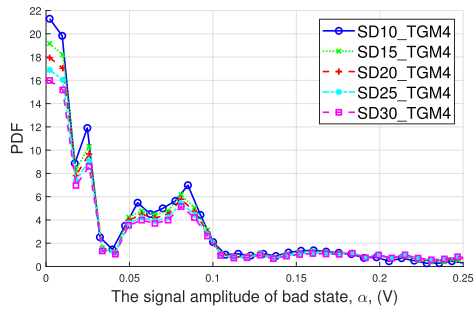
State Duration	SSPV (P)			SPTM (P)		
	10 min	0.882108	0.106909	0.010983	0.996602	0.003375
15 min	0.876565	0.11192	0.011515	0.027765	0.970755	0.00148
				0.002668	0.013607	0.983725
				0.966465	0.032974	0.000562
15 min	0.876565	0.11192	0.011515	0.258561	0.72793	0.013509
				0.039695	0.134351	0.825954



(a) Good state.



(b) Moderate state.



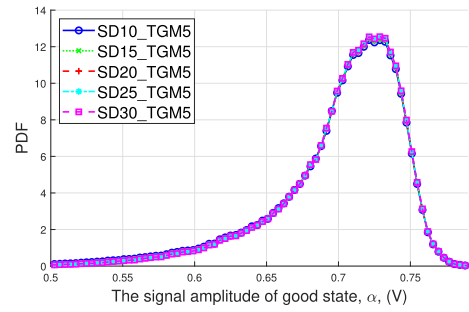
(c) Bad state.

FIGURE 7. The PDFs of signal amplitudes of good state, moderate state and bad state (SD=10, 15, 20, 25, 30 min; TGM=4 dB).

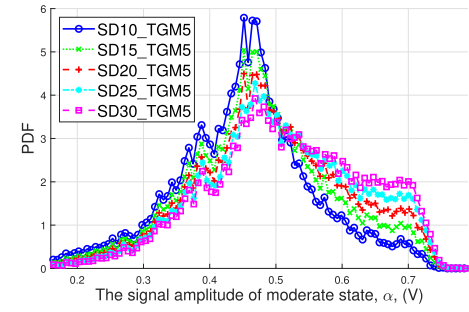
where $\omega = [\omega_1, \omega_2]$, $\mu = [\mu_1, \mu_2]$, and $\delta = [\delta_1, \delta_2]$ denote weight vector, mean vector, and variance vector, respectively. The EM algorithm is used here to estimate parameters of MoG distributions [37].

The EM algorithm for parameter estimation of PDFs of signal amplitudes of good state and moderate state is detailed as follows.

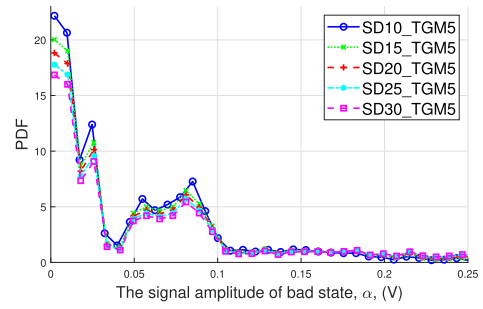
- 1) Initialize $\omega = [\omega_1, \omega_2]$, $\mu = [\mu_1, \mu_2]$, and $\delta = [\delta_1, \delta_2]$.



(a) Good state.



(b) Moderate state.



(c) Bad state.

FIGURE 8. The PDFs of signal amplitudes of good state, moderate state and bad state (SD=10, 15, 20, 25, 30 min; TGM=5 dB).

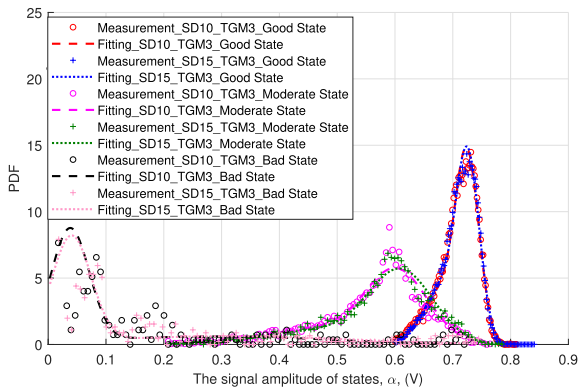
- 2) E step: compute

$$\gamma(m, k) = \frac{\omega_k \mathfrak{N}(\alpha_m; \mu_k, \delta_k)}{\sum_{n=1}^2 \omega_n \mathfrak{N}(\alpha_m; \mu_n, \delta_n)}, \quad \text{for all } k \quad (26)$$

$$\mathfrak{N}(\alpha; \mu, \delta) = \frac{1}{(2\pi)^{\frac{D}{2}}} \frac{1}{|\delta|^{\frac{1}{2}}} e^{-\frac{1}{2}(\alpha-\mu)^T \delta^{-1}(\alpha-\mu)} \quad (27)$$

TABLE 5. The parameters of the mixture of two Gaussian distribution in three states.

State Duration	State	Weight Vector		Mean Vector		Variance Vector	
		ω_1	ω_2	μ_1	μ_2	δ_1	δ_2
10 min	Good State	0.347970392	0.65203	0.68128	0.726409	0.001035	0.000393
	Moderate State	0.296766172	0.703234	0.471615	0.603069	0.010054	0.002856
	Bad State	0.29866231	0.701338	0.290238	0.03809	0.03842	0.001081
15 min	Good State	0.63378441	0.366216	0.727214	0.68443	0.000381	0.000991
	Moderate State	0.743162845	0.256837	0.610572	0.470644	0.003085	0.009401
	Bad State	0.324595203	0.675405	0.313376	0.040384	0.042724	0.001149

**FIGURE 9.** The fitting between MoG distributions and measurement data.

3) M step: update

$$\mu_k = \frac{1}{\sum_{m=1}^N \gamma(m, k)} \sum_{m=1}^N \gamma(m, k) \alpha_m, \quad \text{for all } k \quad (28)$$

$$\delta_k = \frac{1}{\sum_{m=1}^N \gamma(m, k)} \sum_{m=1}^N \gamma(m, k) (\alpha_m - \mu_k) (\alpha_m - \mu_k)^T \quad (29)$$

$$\omega_k = \frac{\sum_{m=1}^N \gamma(m, k)}{N}, \quad \text{for all } k \quad (30)$$

where N is the number of measurement sample.

4) Repeat E step and M step until the convergence condition is met.

The fitted results by the EM algorithm with the measurement data are shown in Fig. 9.

The parameters of the mixture of two Gaussian distribution in three states, such as the weight vector, mean vector, and variance vector, are shown in Table 5.

IV. STATISTICAL PROPERTIES

In this section, the statistical properties of the proposed theoretical channel model in Section II will be derived based on the expressions (12)–(20) under the non-isotropic scattering condition. The statistical properties can capture the effects of the movements of Rx and clusters that in a non-stationarity behavior. There is significant meaning for the satellite communication technology applied in the beyond 5G wireless systems.

A. LOCAL TEMPORAL ACF

The normalized temporal autocorrelation function between two complex fading envelope $h_3(t - \frac{\tau}{2})$ and $h_3(t + \frac{\tau}{2})$ can be presented as

$$\rho(t, \tau) = \frac{E\{h_3^*(t - \frac{\tau}{2})h_3(t + \frac{\tau}{2})\}}{\sqrt{E\{|h_3(t)\}|^2}E\{|h_3(t)\}|^2}} \quad (31)$$

where $(\cdot)^*$ denotes complex conjugate operation and $E\{\cdot\}$ is expectation operator. By substituting (12) and (31), the local temporal ACF can be calculated as

$$\rho(t, \tau) = \rho^{\text{LoS}}(t, \tau) + \rho^{\text{NLoS}}(t, \tau) \quad (32)$$

where the LoS component of the local temporal ACF can be calculated as (33), as shown at the bottom of the next page, and the NLoS components of the local temporal ACF can be calculated as (34), as shown at the bottom of the next page. Please note that $p_\varphi(\varphi^R)$ is the PDF of the AAoA φ^R and $p_\theta(\theta^R)$ is the PDF of the EAoA θ^R . A number of distributions have been adopted to describe the angle parameters, such as the Gaussian distribution [38], the uniform distribution [39], and the Laplacian distribution [40], etc. In this simulation model, the AAoA φ^R and EAoA θ^R are described using the von-Mises distribution [41]. The von-Mises distribution can approximately transform to many distributions [42], which has been successfully validated by measurement data [41]. The PDF of the von-Mises distribution is given by

$$p(\xi) = \frac{e^{\kappa \cos(\xi - \zeta)}}{2\pi I_0(\kappa)}, \quad \xi \in [-\pi, \pi] \quad (35)$$

where $I_0(\cdot)$ is the zero order modified Bessel function of the first kind, ζ is the mean value of the angles, and κ corresponds to the angular spread. The uniform distribution is a special case of the von-Mises distribution when $\kappa = 0$, i.e., $p(\xi) = \frac{1}{2\pi}$. As κ become larger, the angles become more concentrated around the mean value ζ , representing a non-isotropic scattering environment.

B. WIGNER-VILLE SPECTRUM (DOPPLER POWER SPECTRUM DENSITY)

The Wigner-Ville distribution is presented as [43]

$$W(t, f) = \int_{-\infty}^{+\infty} h_3^*(t - \frac{\tau}{2})h_3(t + \frac{\tau}{2})e^{-j2\pi f\tau} d\tau. \quad (36)$$

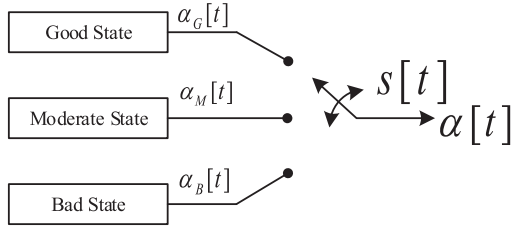


FIGURE 10. Generation of the observed sequence in the Markov-chain-based channel model.

The Wigner-Ville spectrum is the expectation value of the Wigner-Ville distribution, which is the Fourier transform of the local temporal ACF $\rho(t, \tau)$

$$\begin{aligned} S(t, f) &= E\left\{\int_{-\infty}^{+\infty} h_3^*(t - \frac{\tau}{2})h_3(t + \frac{\tau}{2})e^{-j2\pi f\tau} d\tau\right\} \\ &= \int_{-\infty}^{+\infty} \rho(t, \tau)e^{-j2\pi f\tau} d\tau \\ &= S^{\text{LoS}}(t, f) + S^{\text{NLoS}}(t, f) \end{aligned} \quad (37)$$

where the LoS component of the Wigner-Ville spectrum can be calculated as (38), as shown at the bottom of the next page, and the NLoS components of the Wigner-Ville spectrum can be calculated as (39), as shown at the bottom of the next page.

V. SIMULATION RESULTS AND ANALYSIS

In this section, the generation and comparison with measurement data of the received signal area mean power (corresponding FSPL $h_1(t)$ and shadowing $h_2(t)$) are presented. The numerical and simulation results of the received signal local mean statistical properties of (corresponding small-scale fading $h_3(t)$) are also provided. The effects of the movements of Rx is evaluated.

A. RECEIVED SIGNAL AREA MEAN POWER

The Markov process $s[n]$ which represents the switch position in Fig. 10 is obtained by the state transition diagram as depicted in Fig. 2. The initial state is generated by SSPV, and the following states are only determined by the last state and SPTM. We can generate the received amplitude level $\alpha(t)$ by the state chain according to the PDFs of amplitudes of good state, moderate state, and bad state.

To evaluate the performance of simulation, the PDFs of signal amplitudes of good state, moderate state, and bad state in this simulation is calculated and compared with measurement data and the MoG distribution fitting based on EM algorithm in Fig.11.

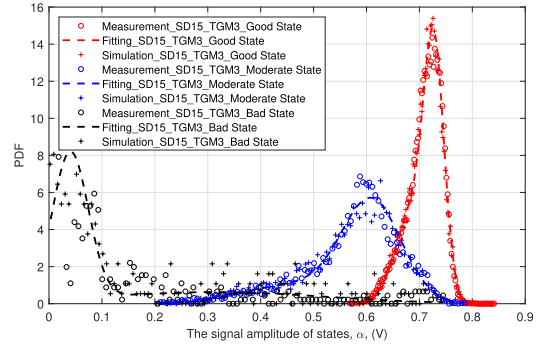


FIGURE 11. The comparison among measurement data, MoG distribution fitting, and simulation.

B. RECEIVED SIGNAL LOCAL MEAN STATISTICAL PROPERTIES

In the proposed theoretical model for small-scale fading, the number of rays is assumed to be infinity ($S \rightarrow \infty$). It is impossible to implement this model directly. With respect to a channel simulator, the simulation model, which is the discrete realization of the theoretical model with a finite number of rays, should be used. The simulation model of the proposed small fading channel model is expressed as

$$h_3(t) = h_3^{\text{LoS}}(t) + h_3^{\text{NLoS}}(t) \quad (40)$$

$$= \underbrace{\sqrt{\frac{K}{K+1}} e^{j(2\pi \int_0^t f^{\text{LoS}}(\tau) d\tau + \phi^{\text{LoS}}(t))}}_{\text{LoS}} \quad (41)$$

$$+ \underbrace{\sqrt{\frac{1}{K+1}} \left(\frac{1}{\sqrt{S}} \sum_{s=1}^S e^{j(\int_0^t f_s^{\text{NLoS}}(\tau) d\tau + \phi_s^{\text{NLoS}}(t))} \right)}_{\text{NLoS}} \quad (42)$$

In the simulation, the modified method of equal areas (MMEA) [44] is adopted to obtain the discrete AAoAs φ_s^R (EAoAs θ_s^R) of finite rays through the following equations

$$\int_{-\pi}^{\varphi_s^R} p(\xi) d\xi = \frac{1}{S} (s - \frac{1}{4}), \quad s = 1, 2, \dots, S, \quad \varphi_s^R \in [-\pi, \pi) \quad (43)$$

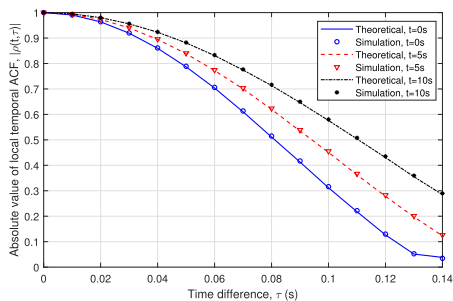
$$\int_0^{\theta_s^R} p(\xi) d\xi = \frac{1}{S} (s - \frac{1}{4}), \quad s = 1, 2, \dots, S, \quad \theta_s^R \in [0, \pi) \quad (44)$$

where $p(\xi)$ is the PDF of von-Mises distribution in (35).

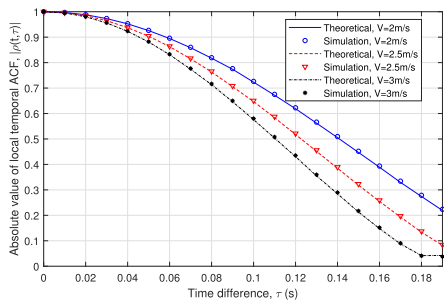
The theoretical and simulated absolute values of the local temporal ACFs with different initial time t are shown

$$\rho^{\text{LoS}}(t, \tau) = \frac{K}{K+1} e^{-j(2\pi \int_0^{t-\frac{\tau}{2}} f^{\text{LoS}}(\varepsilon) d\varepsilon + \phi^{\text{LoS}}(t-\frac{\tau}{2})) + j(2\pi \int_0^{t+\frac{\tau}{2}} f^{\text{LoS}}(\varepsilon) d\varepsilon + \phi^{\text{LoS}}(t+\frac{\tau}{2}))} \quad (33)$$

$$\rho^{\text{NLoS}}(t, \tau) = \frac{1}{K+1} \int_{-\pi}^{\pi} \int_0^{\pi} e^{-j(2\pi \int_0^{t-\frac{\tau}{2}} f^{\text{NLoS}}(\varepsilon) d\varepsilon + \phi^{\text{NLoS}}(t-\frac{\tau}{2})) + j(2\pi \int_0^{t+\frac{\tau}{2}} f^{\text{NLoS}}(\varepsilon) d\varepsilon + \phi^{\text{NLoS}}(t+\frac{\tau}{2}))} p_{\varphi}(\varphi^R) p_{\theta}(\theta^R) d\theta^R d\varphi^R. \quad (34)$$



(a) With different initial time. ($f_c=39.402$ GHz, $\|v\|=3$ m/s, $\|v_c\|=0.5$ m/s)

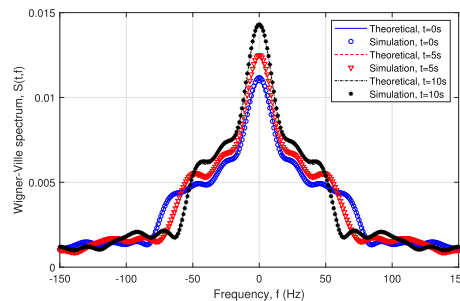


(b) With different velocity of Rx. ($f_c=39.402$ GHz, $t=10$ s, $\|v_c\|=0.5$ m/s)

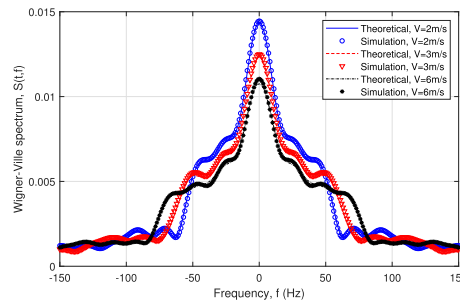
FIGURE 12. The theoretical and simulation absolute value of the local temporal ACFs.

in Fig. 12-(a). The theoretical and simulated results align well, which demonstrates the correctness of our derivation and simulation. The diversity of absolute values of the local temporal ACFs with different initial time shows the non-stationarity of this model. The theoretical and simulated absolute values of the local temporal ACFs with different velocity of Rx (v) are shown in Fig. 12-(b). With a higher speed of Rx, the absolute values of the local temporal ACF drops fast, which can result in a shorter coherence time of the channel.

The theoretical and simulated absolute values of the Wigner-Ville spectrums with different initial time t are shown in Fig. 13-(a). The theoretical and simulation results align well with all selected initial time, which clearly demonstrates that the derivations and simulations are correct. The non-stationarity of this model is also observed through the diversity of Wigner-Ville spectrums with different initial time. The theoretical and simulation absolute values of the Wigner-Ville spectrums with different velocity of Rx (v) are shown in Fig. 13-(b). As velocity of Rx (v) increases,



(a) With different initial time. ($f_c=39.402$ GHz, $\|v\|=3$ m/s, $\|v_c\|=0.5$ m/s)



(b) With different velocity of Rx. ($f_c=39.402$ GHz, $t=10$ s, $\|v_c\|=0.5$ m/s)

FIGURE 13. The theoretical and simulation absolute value of the Wigner-Ville spectrums.

the Wigner-Ville spectrums become more dispersive and the peak value become lower.

VI. CONCLUSION

In this paper, we have proposed a 3D channel model for satellite communications at Q-band in high latitude. It contains three parts, i.e., FSPL model, a modified shadowing model based on a first order Markov-chain process, and a small-scale fading based on GBSM. In the modified shadowing model, the SSPV and SPTM have been calculated by the measurement data. The PDFs of amplitudes of three states (good state, moderate state, and bad state) follow the MoG distribution. The parameters of the MoG distributions are estimated by EM algorithm from the measurement data which is measured on the campus of HWU in Edinburgh, UK. The first order statistical properties of received signal area mean power and the second order received signal local mean statistical properties have been derived and simulated to verify and analyze this model.

$$S^{\text{LoS}}(t, f) = \int_{-\infty}^{+\infty} \frac{K}{K+1} e^{-j\left(2\pi \int_0^{t-\frac{\tau}{2}} f^{\text{LoS}}(\varepsilon) d\varepsilon + \phi^{\text{LoS}}(t-\frac{\tau}{2})\right) + j\left(2\pi \int_0^{t+\frac{\tau}{2}} f^{\text{LoS}}(\varepsilon) d\varepsilon + \phi^{\text{LoS}}(t+\frac{\tau}{2})\right)} e^{-j2\pi f \tau} d\tau \quad (38)$$

$$S^{\text{NLoS}}(t, f) = \int_{-\infty}^{+\infty} \left(\frac{1}{K+1} \int_{-\pi}^{\pi} \int_0^{\pi} e^{-j\left(2\pi \int_0^{t-\frac{\tau}{2}} f^{\text{NLoS}}(\varepsilon) d\varepsilon + \phi^{\text{NLoS}}(t-\frac{\tau}{2})\right) + j\left(2\pi \int_0^{t+\frac{\tau}{2}} f^{\text{NLoS}}(\varepsilon) d\varepsilon + \phi^{\text{NLoS}}(t+\frac{\tau}{2})\right)} \times p_{\varphi}(\varphi^{\text{R}}) p_{\theta}(\theta^{\text{R}}) d\theta^{\text{R}} d\varphi^{\text{R}}\right) e^{-j2\pi f \tau} d\tau. \quad (39)$$

REFERENCES

- [1] C.-X. Wang, F. Haider, X. Gao, X.-H. You, Y. Yang, D. Yuan, H. M. Aggoune, H. Haas, S. Fletcher, and E. Hepsaydir, "Cellular architecture and key technologies for 5G wireless communication networks," *IEEE Commun. Mag.*, vol. 52, no. 2, pp. 122–130, Feb. 2014.
- [2] X. Ge, S. Tu, G. Mao, and C. X. Wang, "5G ultra-dense cellular networks," *IEEE Trans. Wireless Commun.*, vol. 23, no. 1, pp. 72–79, Feb. 2016.
- [3] S. Wu, C.-X. Wang, E. H. M. Aggoune, M. M. Alwakeel, and X. You, "A general 3-D non-stationary 5G wireless channel model," *IEEE Trans. Commun.*, vol. 66, no. 7, pp. 3065–3078, Jul. 2018.
- [4] C.-X. Wang, J. Bian, J. Sun, W. Zhang, and M. Zhang, "A survey of 5G channel measurements and models," *IEEE Commun. Surveys Tuts.*, vol. 20, no. 4, pp. 3142–3168, 4th Quart., 2018.
- [5] T. Wei, W. Feng, J. Wang, N. Ge, and J. Lu, "Exploiting the shipping lane information for energy-efficient maritime communications," *IEEE Trans. Veh. Technol.*, vol. 68, no. 7, pp. 7204–7208, Jul. 2019.
- [6] C. Liu, W. Feng, T. Wei, and N. Ge, "Fairness-oriented hybrid precoding for massive MIMO maritime downlink systems with large-scale CSIT," *China Commun.*, vol. 15, no. 1, pp. 52–61, Jan. 2018.
- [7] *Study on New Radio (NR) to Support Non-Terrestrial Networks*, document TR 38.811, 3GPP, Dec. 2017.
- [8] W. Feng, J. Wang, Y. Chen, X. Wang, N. Ge, and J. Lu, "UAV-aided MIMO communications for 5G Internet of Things," *IEEE Internet Things J.*, vol. 6, no. 2, pp. 1731–1740, Apr. 2019.
- [9] Y. Chen, W. Feng, and G. Zheng, "Optimum placement of UAV as relays," *IEEE Commun. Lett.*, vol. 22, no. 2, pp. 248–251, Feb. 2018.
- [10] T. Qi, W. Feng, and Y. Wang, "Outage performance of non-orthogonal multiple access based unmanned aerial vehicles satellite networks," *China Commun.*, vol. 15, no. 5, pp. 1–8, May 2018.
- [11] A. Molisch, *Wireless Communications*. London, U.K.: Wiley, 2011.
- [12] M. Milojevic, M. Haardt, E. Eberlein, and A. Heuberger, "Channel modeling for multiple satellite broadcasting systems," *IEEE Trans. Broadcast.*, vol. 55, no. 4, pp. 705–718, Dec. 2009.
- [13] M. Pätzold, Y. Li, and F. Laue, "A study of a land mobile satellite channel model with asymmetrical Doppler power spectrum and lognormally distributed line-of-sight component," *IEEE Trans. Veh. Technol.*, vol. 47, no. 1, pp. 297–310, Feb. 1998.
- [14] A. Moro and U. Spagnolini, "Error probability of direct sequence-code division multiple access systems with adaptive antenna minimum mean-square error multiuser receivers in Rayleigh-lognormal fading," *IET Commun.*, vol. 3, no. 10, pp. 1649–1658, Oct. 2009.
- [15] C. Yoon, H. Lee, and J. Kang, "Performance evaluation of space-time block codes from coordinate interleaved orthogonal designs in shadowed fading channels," *IEEE Trans. Veh. Technol.*, vol. 60, no. 3, pp. 1289–1295, Mar. 2011.
- [16] S. Scalise, H. Ernst, and G. Harles, "Measurement and Modeling of the Land Mobile Satellite Channel at Ku-Band," *IEEE Trans. Veh. Technol.*, vol. 57, no. 2, pp. 693–703, Mar. 2008.
- [17] C. Fischione, M. D'Angelo, and M. Butussi, "Utility maximization via power and rate allocation with outage constraints in Nakagami-lognormal channels," *IEEE Trans. Wireless Commun.*, vol. 10, no. 4, pp. 1108–1120, Apr. 2011.
- [18] L.-L. Yang and W. Fang, "Performance of distributed-antenna DS-CDMA systems over composite lognormal shadowing and Nakagami- m -fading channels," *IEEE Trans. Veh. Technol.*, vol. 58, no. 6, pp. 2872–2883, Jul. 2009.
- [19] S. Hazra and A. Mitra, *Advances in Computing and Communications*. Berlin, Germany: Springer, 2011.
- [20] N. Youssef, C.-X. Wang, and M. Pätzold, "A study on the second order statistics of Nakagami-Hoyt mobile fading channels," *IEEE Trans. Veh. Technol.*, vol. 54, no. 4, pp. 1259–1265, Jul. 2005.
- [21] Q. Zhu, X. Dang, D. Xu, and X. Chen, "High efficient rejection method for generating Nakagami- m sequences," *Electron. Lett.*, vol. 47, no. 19, pp. 1100–1101, Sep. 2011.
- [22] H.-P. Lin and M.-C. Tseng, "Modelling fading properties for mobile satellite link channels using non-stationary hidden Markov model," *IET Microw. Antennas Propag.*, vol. 3, no. 1, pp. 171–180, Feb. 2009.
- [23] L. E. Braten and T. Tjelta, "Semi-Markov multistate modeling of the land mobile propagation channel for geostationary satellites," *IEEE Trans. Antennas Propag.*, vol. 50, no. 12, pp. 1795–1802, Dec. 2002.
- [24] E. L. Cid, A. V. Alejos, M. G. Sánchez, and S. G. Fernández, "Statistical model for satellite to helicopter radio channel," in *Proc. 44th Eur. Microw. Conf.*, Rome, Italy, Oct. 2014, pp. 73–76.
- [25] E. Cid, M. G. Sanchez, and A. V. Alejos, "Wideband analysis of the satellite communication channel at Ku- and X-bands," *IEEE Trans. Veh. Technol.*, vol. 65, no. 4, pp. 2787–2790, Apr. 2016.
- [26] W. Fan, P. Kyösti, L. Hentilä, and G. F. Pedersen, "A flexible millimeter-wave radio channel emulator design with experimental validations," *IEEE Trans. Antennas Propag.*, vol. 66, no. 11, pp. 6446–6451, Nov. 2018.
- [27] A. W. Mbugua, W. Fan, Y. Ji, and G. F. Pedersen, "Millimeter wave multi-user performance evaluation based on measured channels with virtual antenna array channel sounder," *IEEE Access*, vol. 6, pp. 12318–12326, 2018.
- [28] H. Fenech, A. Tomatis, S. Amos, J. S. Merino, and V. Soumpholphakdy, "An operator's perspective on propagation," in *Proc. 8th Eur. Conf. Antennas Propag. (EuCAP)*, The Hague, The Netherlands, Apr. 2014, pp. 2164–3342.
- [29] *Path Loss Model for NTN*, document R1-1804479, 3GPP, Nokia, Sanya, China, Apr. 2018.
- [30] *Propagation Data Required for the Design of Earth Space Land Mobile Telecommunication Systems*, document ITU-R P.681, Oct. 2009.
- [31] *Calculation of Free-Space Attenuation*, document ITU-R P.525-3, Sep. 2016.
- [32] J. Huang, C.-X. Wang, R. Feng, J. Sun, W. Zhang, and Y. Yang, "Multi-frequency mmWave massive MIMO channel measurements and characterization for 5G wireless communication systems," *IEEE J. Sel. Areas Commun.*, vol. 35, no. 7, pp. 1591–1605, Jul. 2017.
- [33] J. Nessel, J. Morse, M. Zemba, C. Riva, and L. Luini, "Preliminary results of the NASA beacon receiver for alphasat also paraboni TDP5 propagation experiment," in *Proc. 20th Ka Broadband Commun., Navigat. Earth Observ. Conf.*, Salerno, Italy, Oct. 2014, pp. 1–9.
- [34] M. J. Zemba, J. R. Morse, and J. A. Nessel, "Frequency estimator performance for a software-based beacon receiver," in *Proc. IEEE Antennas Propag. Soc. Int. Symp. (APSURSI)*, Jul. 2014, pp. 1574–1575.
- [35] B. Quinn and J. Fernandes, "A fast efficient technique for the estimation of frequency," *Biometrika*, vol. 78, no. 3, pp. 489–497, Sep. 1991.
- [36] *Digital Video Broadcasting (DVB); Second Generation Framing Structure, Channel Coding and Modulation Systems for Broadcasting, (v1.1.1)*, Standard EN 302 307-2, ETSI, Sophia Antipolis, France, Nov. 2014.
- [37] C. M. Bishop, *Pattern Recognition and Machine Learning*. New York, NY, USA: Springer, 2007.
- [38] P. Ky et al., "WINNER II channel models, WINNER II D1.1.2, v1.2," Tech. Rep. IST-4-027756, Apr. 2008.
- [39] D.-S. Shiu, G. J. Foschini, M. J. Gans, and J. M. Kahn, "Fading correlation and its effect on the capacity of multielement antenna systems," *IEEE Trans. Commun.*, vol. 48, no. 3, pp. 502–513, Mar. 2000.
- [40] *Technical Specification Group Radio Access Network, Study on 3D Channel Model for LTE (Release 12), V12.0.0*, document TR 36.873, 3GPP, Jun. 2015.
- [41] A. Abdi, J. A. Barger, and M. Kaveh, "A parametric model for the distribution of the angle of arrival and the associated correlation function and power spectrum at the mobile station," *IEEE Trans. Veh. Technol.*, vol. 51, no. 3, pp. 425–434, May 2002.
- [42] K. V. Mardia, *Statistics of Directional Data*. London, U.K.: Academic, 1972.
- [43] K. Gröchenig, *Foundations of Time-Frequency Analysis*. New York, NY, USA: Springer, 2013.
- [44] C. A. Gutierrez-Diaz-de-Leon, and M. Pätzold, "Sum-of-sinusoids-based simulation of flat fading wireless propagation channels under non-isotropic scattering conditions," in *Proc. IEEE GLOBECOM*, Washington, DC, USA, Nov. 2007, pp. 3842–3846.
- [45] H. Suzuki, "A statistical model for urban radio propagation," *IEEE Trans. Commun.*, vol. 25, no. 7, pp. 673–680, Jul. COMM-1977.



LU BAI received the B.Sc. degree in electronic information engineering from Qufu Normal University, China, in 2014. She is currently pursuing the Ph.D. degree in information and communication engineering with Shandong University, China. From 2017 to 2019, she is also a Visiting Ph.D. Student with Heriot-Watt University, U.K. Her research interests include massive MIMO channel measurements and modeling, satellite communication channel modeling, and wireless big data.



CHENG-XIANG WANG (S'01–M'05–SM'08–F'17) received the B.Sc. and M.Eng. degrees in communication and information systems from Shandong University, China, in 1997 and 2000, respectively, and the Ph.D. degree in wireless communications from Aalborg University, Denmark, in 2004.

He was a Research Assistant with the Hamburg University of Technology, Hamburg, Germany, from 2000 to 2001, a Visiting Researcher with Siemens AG Mobile Phones, Munich, Germany, in 2004, and a Research Fellow with the University of Agder, Grimstad, Norway, from 2001 to 2005. He has been with Heriot-Watt University, Edinburgh, U.K., since 2005, where he was promoted to Professor, in 2011. In 2018, he joined Southeast University, China, as a Professor. He is also a part-time Professor with Purple Mountain Laboratories, Nanjing, China. He has authored three books, one book chapter, and over 350 articles in refereed journals and conference proceedings, including 23 highly cited articles. He has also delivered 17 invited keynote speeches/talks and seven tutorials in international conferences. His current research interests include wireless channel measurements and modeling, (B)5G wireless communication networks, and applying artificial intelligence to wireless communication networks.

Dr. Wang is a Fellow of the IET, an IEEE Communications Society Distinguished Lecturer, in 2019 and 2020, and a Highly-Cited Researcher recognized by Clarivate Analytics, in 2017 and 2018. He received ten Best Paper Awards from the IEEE GLOBECOM 2010, the IEEE ICCT 2011, ITST 2012, the IEEE VTC 2013-Spring, IWCMC 2015, IWCMC 2016, the IEEE/CIC ICC 2016, WPMC 2016, and WOCC 2019. He has served as a TPC Member, the TPC Chair, and the General Chair for over 80 international conferences. He is currently an Executive Editorial Committee Member of the IEEE TRANSACTIONS ON WIRELESS COMMUNICATIONS. He has served as an Editor for nine international journals, including the IEEE TRANSACTIONS ON WIRELESS COMMUNICATIONS, from 2007 to 2009, the IEEE TRANSACTIONS ON VEHICULAR TECHNOLOGY, from 2011 to 2017, and the IEEE TRANSACTIONS ON COMMUNICATIONS, from 2015 to 2017. He was a Guest Editor of the IEEE JOURNAL ON SELECTED AREAS IN COMMUNICATIONS, Special Issue on Vehicular Communications and Networks (Lead Guest Editor), Special Issue on Spectrum and Energy Efficient Design of Wireless Communication Networks, and Special Issue on Airborne Communication Networks. He was also a Guest Editor of the IEEE TRANSACTIONS ON BIG DATA, Special Issue on Wireless Big Data, and is a Guest Editor of the IEEE TRANSACTIONS ON COGNITIVE COMMUNICATIONS AND NETWORKING, Special Issue on Intelligent Resource Management for 5G and Beyond.



GEORGE GOUSSETIS (S'99–M'02–SM'12) received the Diploma degree in electrical and computer engineering from the National Technical University of Athens, Greece, in 1998, the Ph.D. degree from the University of Westminster, London, U.K., in 2002, and the B.Sc. degree (Hons.) in physics from University College London (UCL), U.K., in 2002. In 1998, he joined Space Engineering, Rome, Italy, as an RF Engineer, and in 1999, he joined the Wireless Communications

Research Group, University of Westminster, U.K., as a Research Assistant. From 2002 to 2006, he was a Senior Research Fellow with Loughborough University, U.K. He was a Lecturer (Assistant Professor) with Heriot-Watt University, Edinburgh, U.K., from 2006 to 2009, and a Reader (Associate Professor) with Queen's University Belfast, U.K., from 2009 to 2013. In 2013, he joined Heriot-Watt University as a Reader and was promoted to Professor, in 2014, where he currently directs the Institute of Sensors Signals and Systems. He has authored or coauthored over 500 peer-reviewed articles, five book chapters, and one book and holds four patents. His research interest includes microwave and antenna components and subsystems. He has held a Research Fellowship from the Onassis Foundation, in 2001, a Research Fellowship from the U.K. Royal Academy of Engineering, from 2006 to 2011, and the European Marie-Curie Experienced Researcher

Fellowships, from 2011 to 2012 and from 2014 to 2017. He was a recipient of the 2011 European Space Agency Young Engineer of the Year Prize, the 2011 EuCAP Best Student Paper Prize, the 2012 EuCAP Best Antenna Theory Paper Prize, and the 2016 Bell Labs prize. He has served as an Associate Editor for the IEEE ANTENNAS AND WIRELESS PROPAGATION LETTERS.



SHANGBIN WU received the B.Sc. degree in communication engineering from South China Normal University, Guangzhou, China, in 2009, the M.Sc. degree (Hons.) in wireless communications from the University of Southampton, Southampton, U.K., in 2010, and the Ph.D. degree in electrical engineering from Heriot-Watt University, Edinburgh, U.K., in 2015. From 2010 to 2011, he was an LTE R&D Engineer responsible for LTE standardization and system-level simulation at New Postcom Equipment Ltd., Guangzhou, China. From October 2011 to August 2012, he was with Nokia Siemens Network, where he was an LTE Algorithm Specialist, mainly focusing on LTE radio resource management algorithm design and system-level simulations. He has been with the Samsung R&D Institute U.K. as a 5G Researcher, since November 2015.



QIUMING ZHU received the B.Sc. degree in electronic engineering from the Nanjing University of Aeronautics and Astronautics (NUAA), Nanjing, China, in 2002, and the M.S. and Ph.D. degrees in communication and information systems, in 2005 and 2012, respectively. Since 2012, he has been an Associate Professor in wireless communications. From 2016 to 2017, he was also a Visiting Academic with Heriot-Watt University. His research interests include channel modeling

for 5G communication systems and wireless channel emulators.



WENQI ZHOU received the B.Sc. degree from Shandong Architecture University, in 2001, and the M.Sc. degree in control science and engineering from Shandong University, in 2006. He has been with Shandong Huahan Electronics Company Ltd., since 2013, and involved in the research of information security, wireless communications, and intelligent robots. His current research interest includes wireless channel characterization and modeling.



EL-HADI M. AGGOUNE (M'83–SM'93) received the M.S. and Ph.D. degrees in electrical engineering from the University of Washington (UW), Seattle, WA, USA. He taught graduate and undergraduate courses in electrical engineering at many universities in the USA and abroad. He served at many academic ranks, including an Endowed Chair Professor. He is currently serving as a Professor and the Director of the SNCS Research Center, University of Tabuk, Saudi Arabia. He is

listed as an Inventor in two patents assigned to the Boeing Company, USA, and the Sensor Networks and Cellular Systems Research Center, University of Tabuk. His research is referred to many patents, including patents assigned to ABB, Switzerland, and EPRI, USA. He has authored many articles in IEEE and other journals and conferences. His research interests include wireless sensor networks, energy systems, and scientific visualization. He is serving on many technical committees for conferences worldwide as well as a reviewer for many journals. One of his laboratories received the Boeing Supplier Excellence Award. He received the IEEE Professor of the Year Award, UW Branch. He is a registered Professional Engineer in the State of Washington.

...